Reconstruction of local heat fluxes in pool boiling experiments along the entire boiling curve from high resolution transient temperature measurements

Yi Heng [a], Adel Mhamdi [a], Sven Groß [b], Arnold Reusken [b],
Martin Buchholz [c], Hein Auracher [c], Wolfgang Marquardt [a,*]

[a] *Process Systems Engineering, RWTH Aachen University, Lehrstuhl für Prozesstechnik,*
Turmstraße 46, D-52064 Aachen, Germany

[b] *Numerical Mathematics, RWTH Aachen University, Lehrstuhl für Numerische Mathematik ,*
Templergraben 55, D-52056 Aachen, Germany

[c] *Institute for Energy Engineering, Berlin University of Technology, Institut für Energietechnik,*
Marchstr. 18, D-10587 Berlin, Germany

Abstract

In this paper, we consider a transient inverse heat conduction problem (IHCP) defined on an irregular three-dimensional (3D) domain in pool boiling experiments. Heat input to a circular copper heater of 35 mm diameter and 7 mm thickness is provided by a resistance heating foil pressed to the bottom of the heater. The heat flux at the inaccessible boiling side is estimated from a number of temperature readings in the heater volume. These temperatures are measured by some high-resolution microthermocouples, which are mounted 3.6 μm below the surface in the test heater. The IHCP is formulated as a mathematical optimization problem and solved by the conjugate gradient (CG) method. The arising PDE problems are solved using the software package "DROPS". A simulation case study is used to validate the performance of the solution approach. Finally, we apply the solution approach to the IHCP in pool boiling experiments. The procedure enables the reconstruction of local instantaneous heat flux distribution on the heater surface at different locations along the boiling curve.

Key words: Inverse heat conduction problem; Pool boiling; Heat flux estimation; Conjugate gradient method; Regularization; Microthermocouple

---

[*] Corresponding author. Tel.: +49 241 80 96712; fax: +49 241 80 92326.
Email address: `wolfgang.marquardt@avt.rwth-aachen.de` (Wolfgang Marquardt).

Preprint submitted to Int. J. of Heat and Mass Transfer *31 October 2007*

Nomenclature

Direct problems

Ω, $\partial\Omega$	3D domain and its boundary	Γ_H	heated boundary of Ω
Γ_B	boiling boundary of Ω	Γ_R	remaining boundary of Ω
Γ_M	measurement plane inside Ω	n	outer normal on $\partial\Omega$
Θ, T, T_d	temperature distribution in Ω	Θ_0	initial temperature distribution
Θ_m, T_m	temperature measurement on Γ_M	q_h	input heat flux on Γ_H
q_b	unknown heat flux on Γ_B	t_f, t'	final and backwards times
λ	thermal conductivity	a	thermal diffusivity
S	sensitivity problem solution	l	adjoint problem solution

Optimization

J	(continuous) objective functional	∇J	gradient of the objective functional
P^n	descent direction (nth iteration)	γ^n	conjugate coefficient (nth iteration)
μ^n	search step length (nth iteration)	$\hat{q}_b{}^n$	estimated heat flux (nth iteration)

Simulation case study

q_b^{ex}	simulated exact heat flux	α	temporally varying term of q_b^{ex}
β	spatially varying term of q_b^{ex}	Θ_m^{ex}	generated error-free measurement data
$J_\#$	(discrete) objective functional	$\lvert\lvert \cdot \rvert\rvert_\#$	solution norm
τ	time step size	ϵ	threshold parameter
ω	measurement error	σ	standard deviation
n_{iter}	number of optimization iterations		

1 Introduction

Boiling heat transfer is hard to model and to predict due to its complex nature [1,2]. During the past decades, many investigations of boiling phenomena have been conducted on the equipment or the macroscale, the meso- and microscopic as well as the molecular scale. The dynamic behavior of a rising bubble plume is a typical phenomenon observed on the macroscale of the heat transfer equipment, e.g. in a boiling vessel. It has been studied extensively both theoretically and experimentally [3–5]. Dhir and Liaw [6] have developed a unifying framework for nucleate and transition boiling on base of a macroscopic geometry model of "vapor stems". Their model assumes that all heat conduced into the liquid adjacent to the surface is used for evaporation at the interface of the vapor stems. On the mesoscale, single bubbles growing on a heated plate or emerging out of the closed film in film boiling have been studied in detail, e.g. [7–9]. On the microscale, the microlayer theory proposed by Stephan and Hammer [10] predicts that most of the heat during boiling is transferred in the micro-region of the three-phase contact line by evaporation. Predicted peak heat fluxes in the microlayer are much larger ($\sim 10^2$) than the macroscopic heat fluxes captured by the boiling curve. However, none of the mentioned approaches have been fully validated yet because of lacking experimental and theoretical evidence. Existing design methods are mostly based on correlations which are valid only for one of the boiling regimes, i.e. nucleate boiling, critical heat flux, transition and film boiling. Boiling heat flux has been considered to be correlated with many different parameters, e.g. superheat, nucleation site density or bubble diameter in the nucleate boiling and average vapor fraction or vapor velocity in transition boiling [11]. It is unclear yet which parameters dominate the boiling heat transfer. A reliable prediction of boiling heat fluxes on a theoretical basis as a function of superheat and other relevant parameters are still not available, especially for higher heat fluxes.

An adequate understanding of the various physical effects can only be obtained if high resolution measurement techniques are employed [12]. One particular technique constitutes of microthermocouples with the tips very near (3.6 μm) to the surface in a test heater. The temperature readings in the heater volume provide indirect information on the surface temperature, the surface heat flux distribution as well as the wetting characteristics on the surface. This kind of experimental approach has been taken in recent years at TU Berlin [12]. Fig. 1 depicts the experimental setup of the test heater with the thermocouple array in the center. The test heater is made from high purity copper and is 7 mm thick. It is cylindrical (diameter 35 mm, 5 mm high) in the top part and quadratic in the bottom part with 38 mm times 38 mm and 2 mm thick with the edges cut off. The heater surface Γ_B is horizontally positioned. Heat flux input q_h is provided by a resistance heating foil, which is pressed on the bottom of the heater. For electrical insulation, a 0.25 mm thick sheet of aluminium nitride is located between foil and heater.

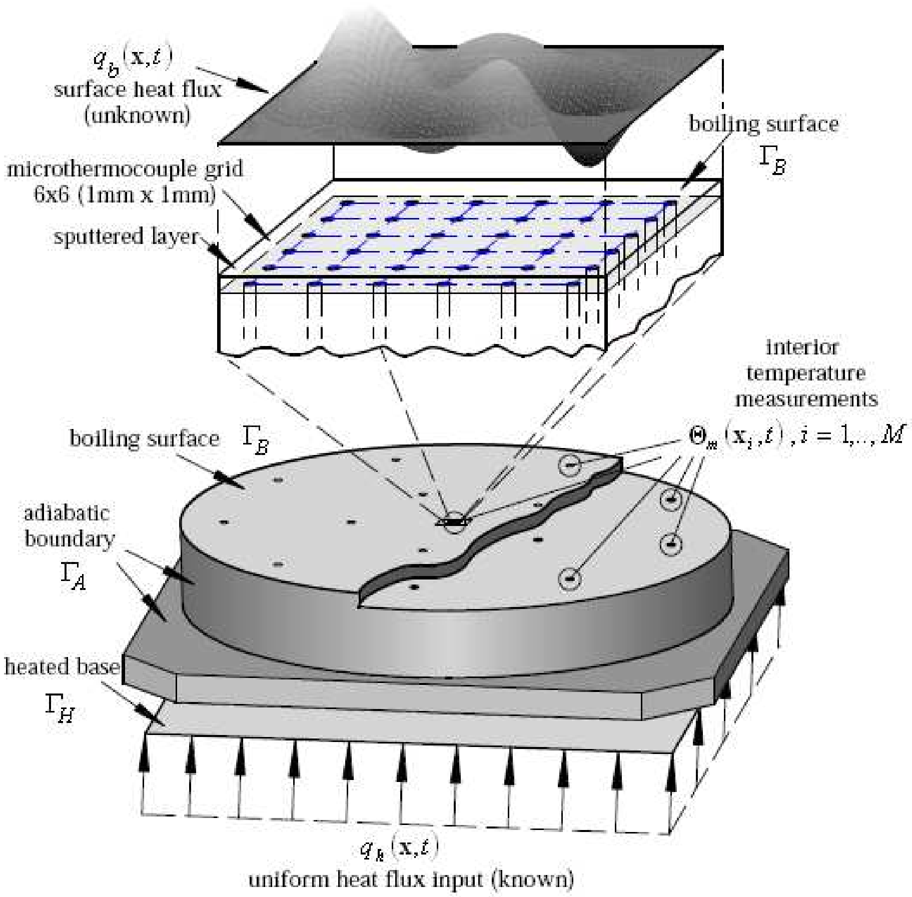

Fig. 1. The test heater and thermocouple tips. (adopted from [13])

In this work, the estimation of the local heat flux q_b on the boiling surface Γ_B from the temperature readings Θ_m in the heater volume is considered. It belongs to the class of IHCPs [14,15], which are ill-posed in the sense of Hadamard [16]. Hadamard gave the definitions of "well-posed problems" and "ill-posed problems" in the early twentieth century. Today, a large number of studies related to IHCPs have already been published. The presented solution methods are mostly based on so-called regularization strategies, e.g. Tikhonov regularization [17], space marching [18], function specification [14] and iterative methods [19]. However, most of them are restricted to one or two space dimensions. Only a few publications are available for IHCPs in three dimensions [20–24]. In [20], an inverse method based on the symbolic approach was proposed to determine the boundary condition in three-dimensional inverse heat conduction problems. The authors in [22] solved the inverse problem using the sequential function specification method with the assumption that future-boundary heat flux varies linearly with time. A filter-based inversion solution method for multi-dimensional IHCPs, which extends the work [25], was presented in [24]. The solution method is based on the interpretation of IHCP in the frequency domain. The authors of [21,23] propose a CG-based iterative regularization method for the solution of 3D IHCPs, which has been applied to the solution of an IHCP in a falling film experiment and obtained good estimation results. In this work, we present a systematic approach that infers the unmeasurable local boiling heat fluxes from point-wise high resolution transient temperature measurements using a mathematical model. We formulate our estimation problems arising from pool boiling experiments for different boiling regimes as 3D IHCPs and solve them by applying a CG-based solution approach. The reconstructed local boiling heat fluxes give a unifying description of the entire boiling curve.

In our previous work, we solved a similar IHCP to estimate the surface heat flux and the surface temperature fields from temperature readings [13,26]. In contrast to this work, only a 2D heat conduction model with unknown boundary conditions at the heater surface has been set up before. The center part of the heater with the microthermocouple array has been partially discretized by means of finite-elements to result in a large system of ordinary differential equations (ODEs). Then linear model reduction techniques [27] were employed to reduce the order of the obtained ODE system. Filter-based inversion algorithms [24] have been constructed and applied to this model. Spatial discretization of the heat conductor in three dimensions results in a much larger system of ODEs, such that the model reduction step becomes computationally intractable.

To overcome the computational difficulties in our filter-based method, we consider in this paper an alternative approach based on the methodology used in [23], where the spatial domain is modelled in 3D. For our problem, an unstructured finite element discretization is applied to the 3D geometry, since the measurement positions are non-uniformly distributed. The boundary conditions are well-defined at those boundaries where no boiling is occurring. This model forms the core of a generalized least-squares problem to minimize an error norm between model predictions and the actual temperature measurements at the thermocouple tips. The inverse problem is solved by an adaptive method involving the CG method for optimization and a multilevel finite-element method for the solution of the arising PDE problems.

The paper is organized as follows. In Section 2, the mathematical formulation of the inverse problem is given. We present a CG-based solution approach in Section 3. In Section 4, we first validate the performance of this solution approach by a simulation case study and then apply it to the real measurement data from the pool boiling experiments. Finally, we give some conclusions about the estimation results and remarks concerning future work.

2 Mathematical formulation of the inverse problem

We consider the general 3D domain Ω shown in Fig. 2, with boundary $\partial\Omega = \Gamma_H \cup \Gamma_B \cup \Gamma_R$, where Γ_H, Γ_B and Γ_R denote the heated boundary, the boiling boundary and the adiabatic boundaries of Ω, respectively. The linear heat conduction problem for the temperature $\Theta(\mathbf{x}, t)$ is given by

$$
\begin{aligned}
&\frac{\partial\Theta(\mathbf{x},t)}{\partial t} = \nabla \cdot (a(\mathbf{x})\nabla\Theta(\mathbf{x},t)), \quad (\mathbf{x},t) \in \Omega \times [0,t_f], && (1)\\
&\Theta(\mathbf{x},0) = \Theta_0(\mathbf{x}), \quad \mathbf{x} \in \Omega, && (2)\\
&-\lambda(\mathbf{x})\frac{\partial\Theta(\mathbf{x},t)}{\partial n} = q_h(\mathbf{x},t), \quad (\mathbf{x},t) \in \Gamma_H \times [0,t_f], && (3)\\
&-\lambda(\mathbf{x})\frac{\partial\Theta(\mathbf{x},t)}{\partial n} = q_b(\mathbf{x},t), \quad (\mathbf{x},t) \in \Gamma_B \times [0,t_f], && (4)\\
&-\lambda(\mathbf{x})\frac{\partial\Theta(\mathbf{x},t)}{\partial n} = 0, \quad (\mathbf{x},t) \in \Gamma_R \times [0,t_f], && (5)
\end{aligned}
$$

where thermal conductivity $\lambda \equiv \lambda(\mathbf{x})$ and thermal diffusivity $a \equiv a(\mathbf{x})$ are functions of the spatial coordinates $\mathbf{x}$. The final time is denoted by t_f. The outer normal on the boundaries is denoted by n.

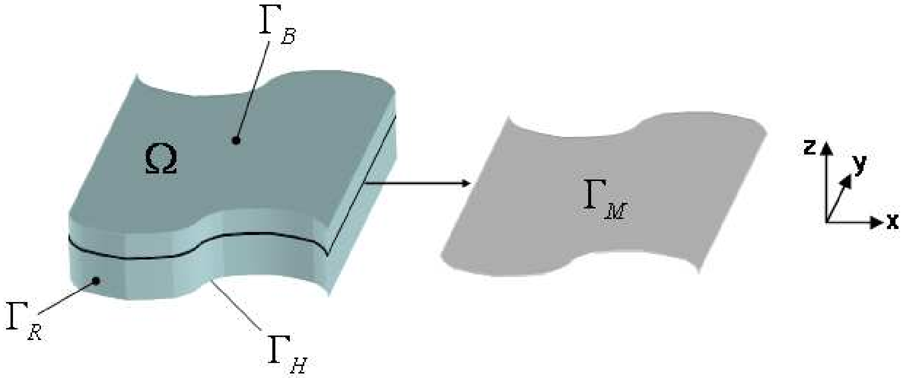

Fig. 2. The general 3D geometry and coordinates.

The inverse problem corresponds to the estimation of the unknown heat flux $q_b(\mathbf{x}, t)$ on Γ_B using temperature measurements $\Theta_m(\mathbf{x}, t)$ on Γ_M, which are obtained by interpolating the pointwise temperature measurement $\Theta_m(\mathbf{x}_i, t)$ as shown in Fig. 1. In this work, only a control volume which covers the 6×6 microthermocouple (MTC) grid at the center of the heater is considered. Since there are no experimental data for the initial temperature distribution Θ_0 available and the values of measured temperatures at the first time instant are almost the same at the measurement positions, their average value is employed as an estimate for $\Theta_0(\mathbf{x})$. Errors in this estimate will result in an unsatisfactory estimation at the first several time instants, however an overall good estimation quality throughout the whole time interval can be ensured. The heat flux input q_h was measured in the experiments and its values are almost stationary and uniformly distributed in space, hence we use a constant approximation in space and time for the computation. Zero heat flux is assumed at the remaining lateral boundaries Γ_R due to a lack of better information.

Due to the linearity, the equations (1)-(5) can be divided into a direct problem:

$$\frac{\partial T_d(\mathbf{x},t)}{\partial t} = \nabla \cdot (a(\mathbf{x}) \nabla T_d(\mathbf{x},t)), \quad (\mathbf{x},t) \in \Omega \times [0, t_f], \tag{6}$$

$$T_d(\mathbf{x},0) = \Theta_0(\mathbf{x}), \quad \mathbf{x} \in \Omega, \tag{7}$$

$$-\lambda(\mathbf{x}) \frac{\partial T_d(\mathbf{x},t)}{\partial n} = q_h(\mathbf{x},t), \quad (\mathbf{x},t) \in \Gamma_H \times [0, t_f], \tag{8}$$

$$-\lambda(\mathbf{x}) \frac{\partial T_d(\mathbf{x},t)}{\partial n} = 0, \quad (\mathbf{x},t) \in \Gamma_B \times [0, t_f], \tag{9}$$

$$-\lambda(\mathbf{x}) \frac{\partial T_d(\mathbf{x},t)}{\partial n} = 0, \quad (\mathbf{x},t) \in \Gamma_R \times [0, t_f], \tag{10}$$

with known initial and boundary conditions and the remaining problem:

$$\frac{\partial T(\mathbf{x},t)}{\partial t} = \nabla \cdot (a(\mathbf{x}) \nabla T(\mathbf{x},t)), \quad (\mathbf{x},t) \in \Omega \times [0, t_f], \tag{11}$$

$$T(\mathbf{x},0) = 0, \quad \mathbf{x} \in \Omega, \tag{12}$$

$$-\lambda(\mathbf{x}) \frac{\partial T(\mathbf{x},t)}{\partial n} = 0, \quad (\mathbf{x},t) \in \Gamma_H \times [0, t_f], \tag{13}$$

$$-\lambda(\mathbf{x}) \frac{\partial T(\mathbf{x},t)}{\partial n} = q_b(\mathbf{x},t), \quad (\mathbf{x},t) \in \Gamma_B \times [0, t_f], \tag{14}$$

$$-\lambda(\mathbf{x}) \frac{\partial T(\mathbf{x},t)}{\partial n} = 0, \quad (\mathbf{x},t) \in \Gamma_R \times [0, t_f], \tag{15}$$

with the unknown boundary condition $q_b(\mathbf{x}, t)$ and vanishing initial condition.

The temperatures Θ, T_d, T in the problems (1)-(5), (6)-(10) and (11)-(15), respectively, are related by

$$\Theta(\mathbf{x},t) = T_d(\mathbf{x},t) + T(\mathbf{x},t), \quad (\mathbf{x},t) \in \Omega \times [0, t_f].$$

With this decomposition, the inverse problem mentioned above is equivalent to estimate q_b in (11)-(15) using measurement data T_m, which are obtained by subtracting the solution $T_d(\mathbf{x},t)$ of the direct problem (6)-(10) on Γ_M from the original temperature measurement $\Theta_m(\mathbf{x},t)$, i.e.

$$T_m(\mathbf{x},t) = \Theta_m(\mathbf{x},t) - T_d(\mathbf{x},t), \quad (\mathbf{x},t) \in \Gamma_M \times [0,t_f].$$

3 Optimization-based solution approach

The direct problem (6)-(10) is computed using the software package DROPS [28]. The solution of the considered inverse problem for q_b is obtained by minimizing the objective functional

$$J(q_b) := \int_0^{t_f} \int_{\Gamma_M} [T(\mathbf{x},t;q_b) - T_m(\mathbf{x},t)]^2 d\mathbf{x}\, dt, \tag{16}$$

where $T(\mathbf{x},t;q_b)$ refers to the temperature field determined as the solution of the problem (11)-(15) for a certain q_b.

The optimization problem (16) is solved by applying a standard iterative optimization algorithm presented in [21,23], where the CG method [29,30] was used to estimate the unknown quantities q_b sequentially until a certain stopping condition is fulfilled.

3.1 The CG iteration

The CG iterative process to calculate an estimate $\hat{q}_b^{n+1}$ of q_b is:

$$\hat{q_b}^{n+1}(\mathbf{x},t) = \hat{q_b}^{n}(\mathbf{x},t) - \mu^n P^n(\mathbf{x},t), \text{ for } n = 0,1,2,... \tag{17}$$

We choose $\hat{q_b}^0 = 0, P^0 = \nabla J^0$ as initial guesses. μ^n is the search step length in iteration n. The conjugate search direction $P^n(\mathbf{x},t)$ is updated by

$$P^n(\mathbf{x},t) = \nabla J^n(\mathbf{x},t) + \gamma^n P^{n-1}(\mathbf{x},t). \tag{18}$$

The corresponding conjugate coefficient γ^n, $n \geq 1$, is determined from

$$\gamma^n = \frac{\int_0^{t_f} \int_{\Gamma_B} [\nabla J^n]^2 d\mathbf{x}\, dt}{\int_0^{t_f} \int_{\Gamma_B} [\nabla J^{n-1}]^2 d\mathbf{x}\, dt}, \tag{19}$$

and $\gamma^0 = 0$.

At each iteration step, there are two quantities to be evaluated, namely μ^n and the gradient ∇J^n. Their determination requires to solve the so-called sensitivity and adjoint problems [15]. The iterative CG-process ends when a certain given stopping condition is fulfilled.

3.2 The sensitivity problem

The sensitivity problem is derived by standard arguments. It is assumed that a variation δq_b of q_b results in a perturbation δT of T. In order to simplify notation, we denote δT by S in the following. Replacing q_b by $q_b + \delta q_b$ and T by $T + S$ in (11)-(15), then subtracting the original direct problem, we obtain the sensitivity problem

$$\frac{\partial S(\mathbf{x},t)}{\partial t} = \nabla \cdot (a(\mathbf{x}) \nabla S(\mathbf{x},t)), \quad (\mathbf{x},t) \in \Omega \times [0,t_f], \tag{20}$$

$$S(\mathbf{x},0) = 0, \quad \mathbf{x} \in \Omega, \tag{21}$$

$$-\lambda(\mathbf{x}) \frac{\partial S}{\partial n}(\mathbf{x},t) = 0, \quad (\mathbf{x},t) \in \Gamma_H \times [0,t_f], \tag{22}$$

$$-\lambda(\mathbf{x}) \frac{\partial S}{\partial n}(\mathbf{x},t) = \delta q_b(\mathbf{x},t), \quad (\mathbf{x},t) \in \Gamma_B \times [0,t_f], \tag{23}$$

$$-\lambda(\mathbf{x}) \frac{\partial S}{\partial n}(\mathbf{x},t) = 0, \quad (\mathbf{x},t) \in \Gamma_R \times [0,t_f], \tag{24}$$

and the search step length

$$\mu^n = \frac{\int_0^{t_f} \int_{\Gamma_M} [T(\mathbf{x},t;\hat{q_b}^n) - T_m(\mathbf{x},t)] S(\mathbf{x},t) d\mathbf{x}\, dt}{\int_0^{t_f} \int_{\Gamma_M} [S(\mathbf{x},t)]^2 d\mathbf{x}\, dt}.$$

In the software implementation, δq_b is replaced by P^n in each iteration n.

3.3 The adjoint problem

To get an expression for the gradient ∇J^n, we define a modified objective functional by adding a term involving an adjoint function $l(\mathbf{x},t)$ to (16), i.e.,

$$\begin{aligned} J(q_b) = {} & \int_0^{t_f} \int_{\Gamma_M} [T(\mathbf{x},t;q_b) - T_m(\mathbf{x},t)]^2 d\mathbf{x}\, dt \\ & + \int_0^{t_f} \int_{\Omega} l(\mathbf{x},t) \{\nabla \cdot (a(\mathbf{x}) \nabla T(\mathbf{x},t;q_b)) - \frac{\partial T(\mathbf{x},t;q_b)}{\partial t}\} d\mathbf{x}\, dt. \end{aligned} \tag{25}$$

Applying calculus of variations, we obtain the adjoint problem

$$\begin{aligned} \frac{\partial l(\mathbf{x},t)}{\partial t} &= -\nabla \cdot (a(\mathbf{x})\nabla l(\mathbf{x},t)) - f(\mathbf{x},t), \quad (\mathbf{x},t) \in \Omega \times [0,t_f], && (26)\\ l(\mathbf{x},t_f) &= 0, \quad \mathbf{x} \in \Omega, && (27)\\ -\lambda(\mathbf{x})\frac{\partial l(\mathbf{x},t)}{\partial n} &= 0, \quad (\mathbf{x},t) \in \partial\Omega \times [0,t_f], && (28) \end{aligned}$$

where $\partial\Omega$ denotes the boundary of Ω and $f \equiv f(\mathbf{x},t)$ is given by

$$f(\mathbf{x},t) = \begin{cases} 2[T(\mathbf{x},t) - T_m(\mathbf{x},t)], & (\mathbf{x},t) \in \Gamma_M \times [0,t_f]; \\ 0, & (\mathbf{x},t) \in \Omega \setminus \Gamma_M \times [0,t_f]. \end{cases}$$

The gradient follows from

$$\nabla J(\mathbf{x},t)|_{\Gamma_B} = [-\frac{a(\mathbf{x})}{\lambda(\mathbf{x})} \cdot l(\mathbf{x},t)]_{|\Gamma_B}.$$

The non-zero property of λ guarantees that the above identity is well-defined. Hence the solution of the adjoint problem results in values of $\nabla J|_{\Gamma_B}$.

The problem (26)-(28) is a final-time value problem. By introducing a new time variable $t' = t_f - t$, it can be transformed to an initial value problem, which can be solved by DROPS. Since our temperature measurements are taken inside the heater volume and not on the boundary, the formulation of the adjoint problem here is different from that in [23].

4 IHCP in pool boiling

In this section, we focus on a particular IHCP defined in a control volume covering thirty-six MTCs in pool boiling experiments [12]. These MTCs have been arranged on an approximately 1×1 mm^2 sized quadratic grid at the center of the heater and 3.6 μm below the heater surface. They are able to resolve the temperature fluctuations with sufficient accuracy with respect to spatial and temporal dimension. Each thermocouple consists of an insulated constantan thermocouple wire (ϕ 38 μm) which is embedded in the heater. A copper layer of 2.5 μm thickness is sputtered on the surface to create a T-type thermocou-

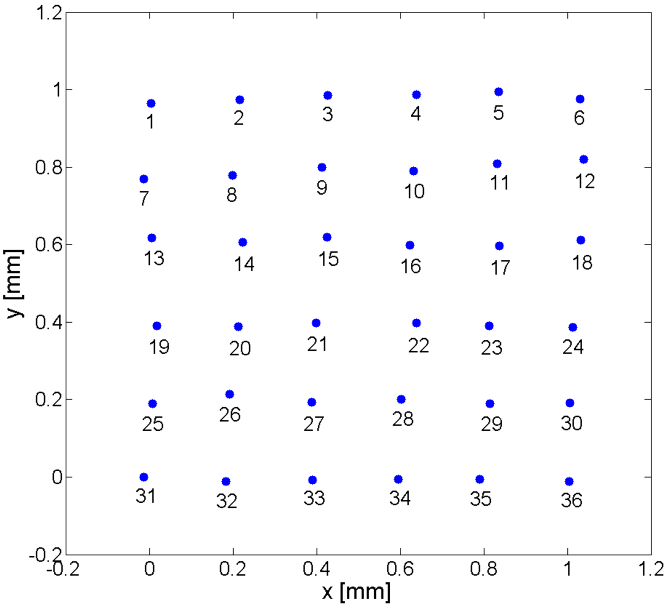

Fig. 3. Measured positions of 1 × 1 mm MTC array (adopted from [12])

ple. The thermocouple wires below the surface do not influence the surface characteristics [12]. The schematic setup of the MTCs and the test heater section are depicted in Fig. 1. The heater surface is coated with a pure gold layer of 1 μm thickness to prevent corrosion and oxidation of the surface. As diffusion resistance a titanium layer of 0.1 μm thickness is located between the copper layer and the gold layer.

The real XY-positions of all MTCs were determined using a calibrated microscope measurement system [12]. The result for all 36 MTCs is shown in Fig. 3. Based on this experimental setup, we define the irregular 3D heater volume shown in Fig. 4 which has approximately the size 1 × 1 × 0.3 mm^3 (in the direction x, y and z, respectively).

The discretization of the heater volume is performed with tetrahedral linear finite elements and the positions of the 36 MTCs are located at grid vertices. The MTCs 1-6, 7, 12, 13, 18, 19, 24, 25, 30 and 31-36 form the boundary of Γ_M. Besides, the mesh refinement also considers the dimension of the thin gold and copper layer which are sputtered on top of the heater to form the boiling surface. The titanium layer is neglected. The mesh of the heater volume (see Fig. 4) from Γ_B to Γ_H is taken increasingly coarser due to the fact that the variation of the temperature distribution in the heater volume decreases rapidly as the location approaches Γ_H. This unstructured discretization results in 2779 spatial unknowns and 12940 tetrahedra. Referring to the general 3D geometry shown in Fig. 2, here $\Gamma_B = \{(x, y, z) \in \Omega, z = 0.3 \text{ mm}\}$, $\Gamma_H = \{(x, y, z) \in \Omega, z = 0 \text{ mm}\}$ and the temperature measurements are taken on $\Gamma_M = \{(x, y, z) \in \Omega, z = 0.2964 \text{ mm}\}$ (3.6 μm below the surface Γ_B). Γ_R corresponds to the remaining boundaries of Ω.

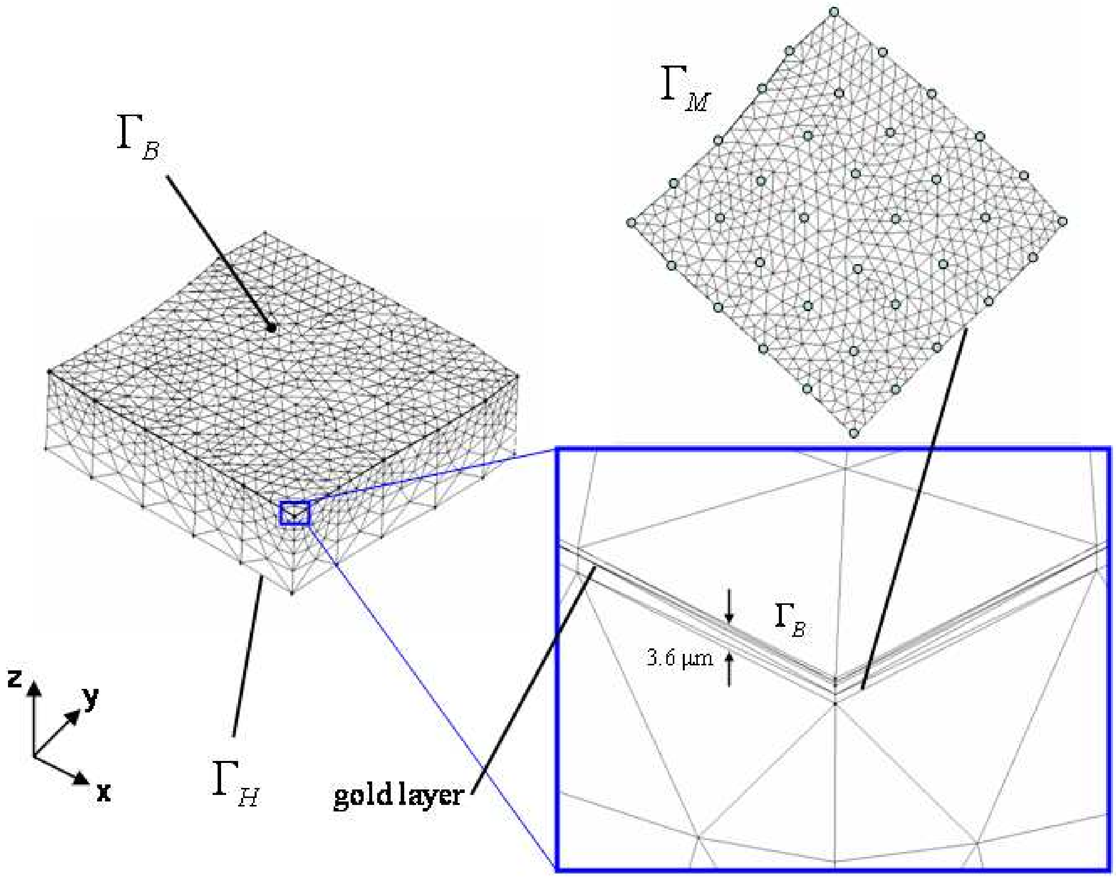

Fig. 4. Discretization model of the 3D heater volume.

Before processing the experimental data (see Section 4.2), a simulation case study is set up in the following section to validate and assess the performance of the solution approach.

4.1 Simulation case study

In this simulation case study, the solution of the direct 3D heat conduction equations is computed using the software package DROPS [28], which is based on multilevel nested finite element discretization methods. The simulation time interval is chosen as $0 \leq t \leq 1$ ms. For the time discretization, an one step θ-scheme [31] with a step size $\tau = 0.01$ ms is used. In this paper we choose $\theta = 0.5$, which leads to the Crank-Nicholson scheme. Piecewise linear finite elements on a tetrahedral grid are employed for the space discretization [32]. The resulting discrete systems of equations are solved with a preconditioned Krylov subspace method [33]. The parameters $a = 0.115$ mm^2/ms and $\lambda = 0.4$ W/mm·K are applied. The initial and known boundary conditions consist of a constant temperature distribution $\Theta(\mathbf{x}, 0) = 40\ °C$ and a constant heat flux $q_h(\mathbf{x}, t) = 0.1$ W/mm^2. For the initialization of the optimization procedure, we choose $\hat{q}_b{}^0(\mathbf{x}, t) = 0, \quad (\mathbf{x}, t) \in \Gamma_B \times [0, 1]$.

The heat flux

$$q_b^{ex}(x, y, t) = \alpha(t) \cdot \beta(x, y), \quad (x, y, t) \in \Gamma_B \times [0, 1]$$

is chosen for this study to simulate the dynamics of a heat flux peak on the heater surface. The spatially and temporally varying terms are

$$\alpha(t) = \begin{cases} 7.5t - 3, & t \in [0, 0.4), \\ 18 sin(5\pi t), & t \in [0.4, 0.61), \\ 4.6559t - 5.6559, & t \in [0.61, 1] \end{cases}$$

and

$$\beta(x, y) = \begin{cases} 0, & \sqrt{(x-0.6)^2 + (y-0.4)^2} > 0.35, \\ \sqrt{0.35^2 - (x-0.6)^2 - (y-0.4)^2}, & \sqrt{(x-0.6)^2 + (y-0.4)^2} \le 0.35. \end{cases}$$

The functions α and β are illustrated in Fig. 5.

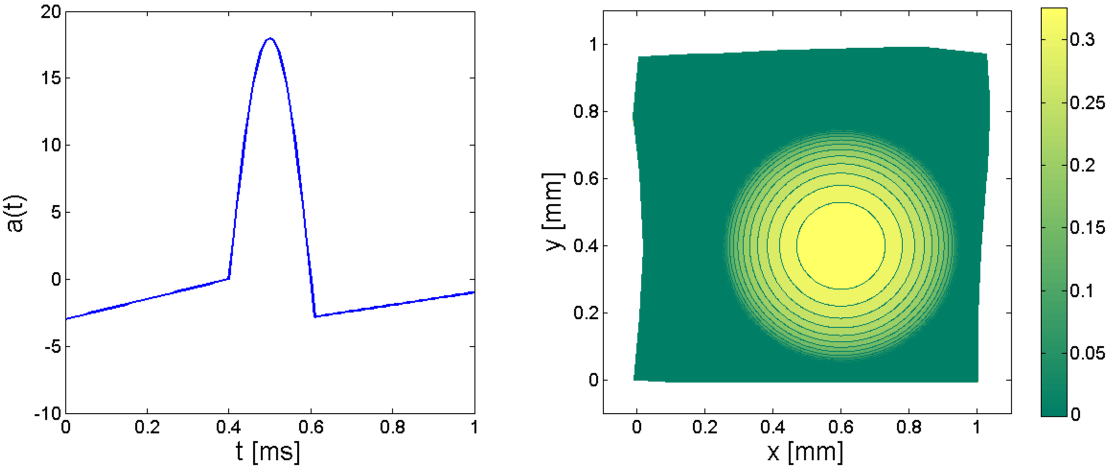

Fig. 5. The functions α (left) and β (right).

4.1.1 Estimation with error-free measurements

In this subsection, we present the estimation results with error-free measurements. We take the temperature Θ_m^{ex} on Γ_M obtained from the solution of the direct problem with the known boundary condition q_b^{ex} as error-free measurement data. A discrete version of the objective functional (16),

$$J_{\#}(\hat{q}_b{}^n) := \sum_{i=1}^{N_t} \sum_{j=1}^{N_m} \frac{1}{N_m} [T(\mathbf{x}_j, t_i; \hat{q}_b{}^n) - T_m(\mathbf{x}_j, t_i)]^2 \cdot \tau, \tag{29}$$

is evaluated, where N_t, N_m denote the number of time steps and mesh points on Γ_M, respectively. t_i are the time instants uniformly discretized with time step size τ in the estimation time interval and $\mathbf{x}_j \in \Gamma_M$ are the corresponding spatial coordinates of the mesh points. n denotes the number of iteration steps in the optimization procedure. Fig. 6 gives a plot of the objective functional over the optimization iterations and it shows that the objective converges rapidly by applying the CG method.

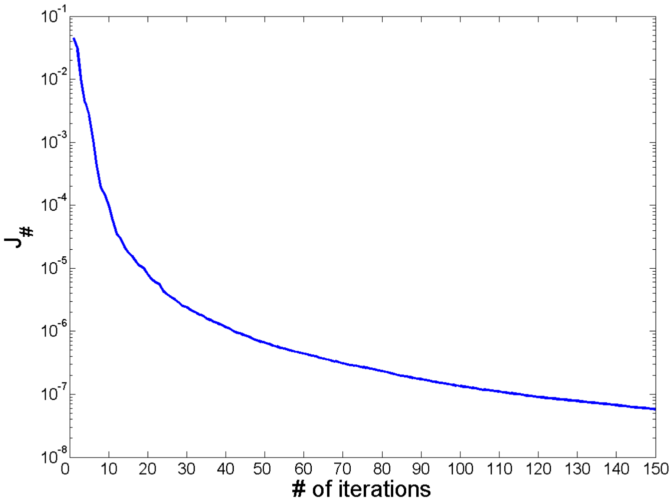

Fig. 6. Convergence behavior.

The contour plots of estimated surface heat fluxes at time instant $t = 0.5$ ms for optimization iterations $n_{iter} = 11$ and $n_{iter} = 150$ are shown in Fig. 7. The peak value of the exact heat flux occurs at this time instant. 36 points positioned exactly above the 36 MTCs (see Fig. 3) are selected on Γ_B to observe the estimated heat flux $\hat{q}_b$ over time t. Fig. 8 shows the estimation results at two positions above the location of MTC 8 and 22 for different number of optimization iterations n_{iter}. The exact heat flux above MTC 8 is zero, while the one above MTC 22 undergoes a big variation over time. The estimated heat fluxes above the other 34 MTCs show a similar quality. Since we use error-free measurement data, the quality of overall estimation result could be improved using more optimization iterations.

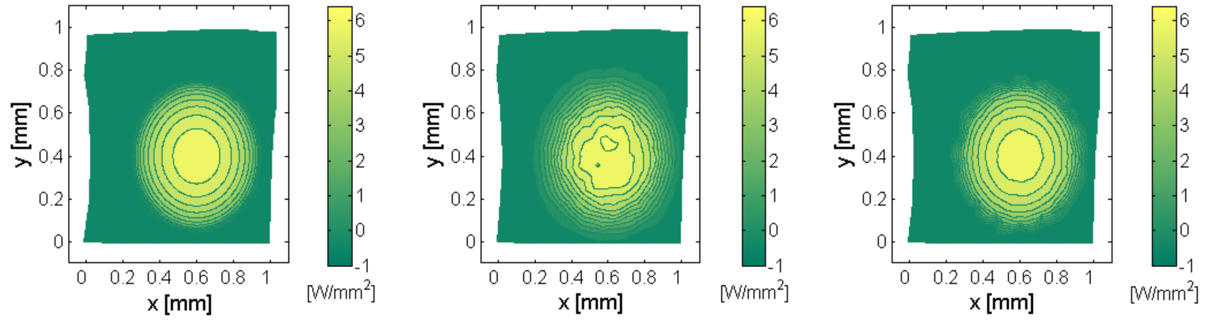

Fig. 7. Contour plots of the exact (left), estimated heat flux for $n_{iter} = 11$ (middle) and estimated heat flux for $n_{iter} = 150$ (right) at time instant $t = 0.5$ ms.

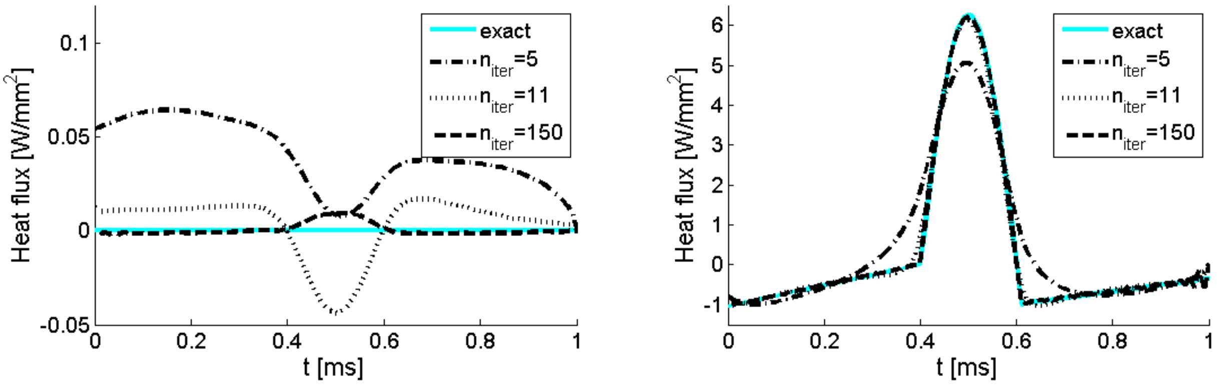

Fig. 8. Estimated surface heat flux $\hat{q}_b$ above position of MTC 8 (left) and of MTC 22 (right) for different number of optimization iterations n_{iter}.

From Fig. 7 we can observe that the estimated heat fluxes oscillate near the boundary of the circle (center: $(0.6, 0.4)$, radius: 0.35) as the number of optimization iterations increases. This is due to the fact that the function of the exact heat flux is not differentiable on the boundary of the region where function β is non-zero. Using a global higher space resolution could decrease the oscillation of estimates near the circle boundary and hence obtain better approximation quality. However, this will also result in higher computation time. Instead of refining the whole grid, a method involving local grid refinement may be preferred. This issue will be investigated in future work.

4.1.2 Estimation in the presence of measurement errors

The simulated measurement data are constructed by perturbing the exact temperature Θ_m^{ex}, obtained as in the previous section, with an artificial measurement error ω. The perturbed measurement temperature Θ_m is given by

$$\Theta_m = \Theta_m^{ex} + \sigma\omega,$$

where σ is the standard deviation of the measurement error. ω is generated from a zero mean normal distribution with variance one. In this simulation case study, we choose $\sigma = 0.02$, which results in a measurement error of approximately 10%.

In case of error corrupted temperature measurements, the estimation quality will become worse if too many iterations are applied, although the value of the objective functional is still getting smaller. This is an indication of fitting the noise due to an overparameterization of the heat flux function representation. In order to find the best termination index, we need a suitable stopping criterion which can be based on the well-known discrepancy principle or the L-curve criterion [29,34].

Discrepancy principle & L-curve criterion

A suitable choice for a stopping criterion is a threshold for the objective functional, i.e.

$$J_{\#}(\hat{q_b}^n) < \epsilon. \tag{30}$$

The discrepancy principle suggests to stop the optimization procedure when the temperature residual matches roughly the error magnitude, i.e.

$$|T(\mathbf{x}_i, t; \hat{q_b}^n) - T_m(\mathbf{x}_i, t)| \approx \sigma. \tag{31}$$

By substituting (31) and (30) into (29) we obtain

$$\epsilon \approx \sigma^2 t_f. \tag{32}$$

The application of this version of the discrepancy principle yields the best termination index — iteration 12.

An alternative method for the choice of the best termination index is the L-curve criterion [29,34], a heuristic rule, which uses a parameterized plot of the objective functional against a solution norm. In this simulation case study, we select the solution norm

$$||\hat{q_b}^n||_{\#}^2 := \sum_{i=1}^{N_t} \sum_{j=1}^{N_b} \frac{1}{N_b} [\frac{d^2 \hat{q_b}^n(\mathbf{x}_j, t)}{dt^2}|_{t=t_i}]^2 \cdot \tau, \tag{33}$$

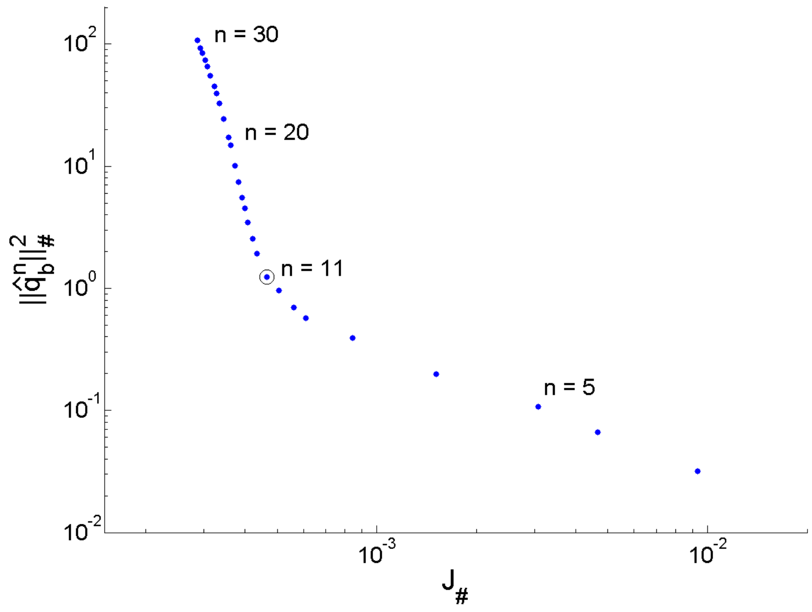

Fig. 9. L-curve for estimation with perturbed measurements with error level $\sigma = 0.02$.

where N_t, N_b denote the number of time steps and mesh points on Γ_B, respectively. $\mathbf{x}_j \in \Gamma_B$ are the corresponding spatial coordinates of the mesh points. The best compromise for the heat flux estimation is found at the maximum curvature of the L-curve as shown in Fig. 9. This maximum curvature arises at iteration 11.

The best termination index obtained by L-curve is very close to the one obtained by the discrepancy principle. Moreover, in case the noise level of the measurement data is not known in advance, the L-curve criterion is a better choice, because it does not require any knowledge on the character of the measurement noise.

Estimation results

The contour plots of optimal ($n_{iter} = 11$) and overestimated ($n_{iter} = 150$) heat fluxes for $t = 0.5$ ms are shown in Fig. 10. Fig. 11 shows the estimation results above positions of MTC 8 and of MTC 22 for different number of optimization iterations n_{iter}.

In contrast to the results shown in Fig. 8, the estimated heat flux above position of MTC 8 already starts to oscillate in the first few iterations in a small range of values (see left top row of Fig. 11), whereas the estimated heat flux above position of MTC 22 has not yet been well approximated and continues to approach the exact one (see left bottom row of Fig. 11). A similar shape pattern of the estimated heat fluxes above position of MTC 8 at iteration 5 shown in Fig. 8 (left) and Fig. 11 (left top row) can be observed, although the latter oscillates. The optimal estimated heat flux is obtained at iteration 11. It captures the major dynamics of the exact heat flux. For longer iterations, the estimated heat flux oscillates and the estimation quality decreases rapidly as further iterations are performed. The overestimated heat flux obtained in iteration 150 strongly oscillates over time and space. It is very different from the exact one. This effect is due to the ill-posedness of the considered IHCP.

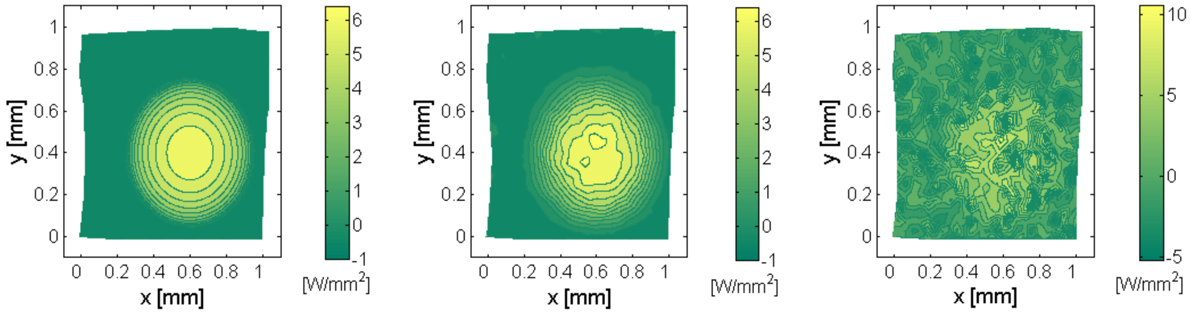

Fig. 10. Contour plots of the exact (left), optimal estimated heat flux (middle) and overestimated heat flux (right) at time instant $t = 0.5$ ms.

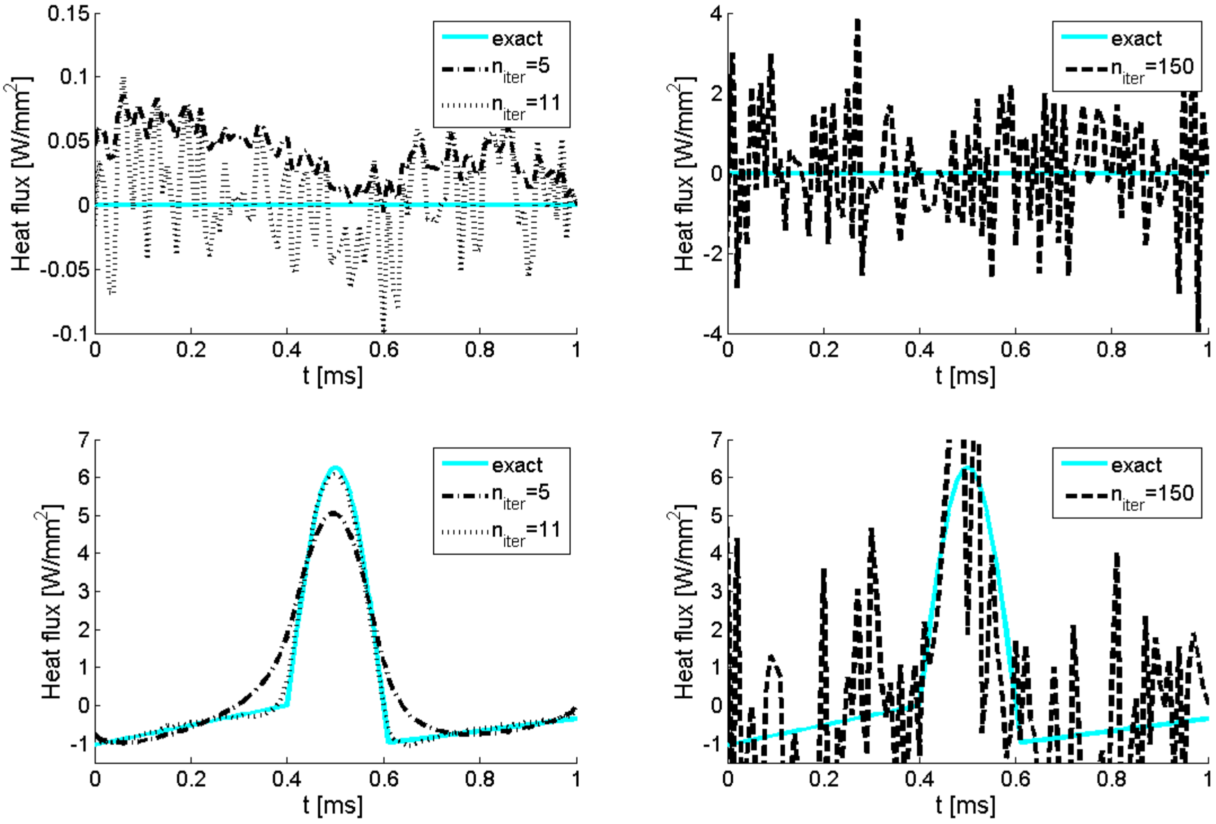

Fig. 11. Estimated surface heat flux $\hat{q}_b$ above position of MTC 8 (top row) and of MTC 22 (bottom row) for different number of optimization iterations n_{iter}.

In the experiment carried out at TU Berlin [12], local processes in pool boiling along the entire boiling curve have been investigated. Using a temperature controlled heater, boiling curves for some test fluids have been evaluated [12,35]. In this section, we use the obtained temperature measurement inside the heater to estimate the local heat flux q_b at the fluid/heater interface Γ_B.

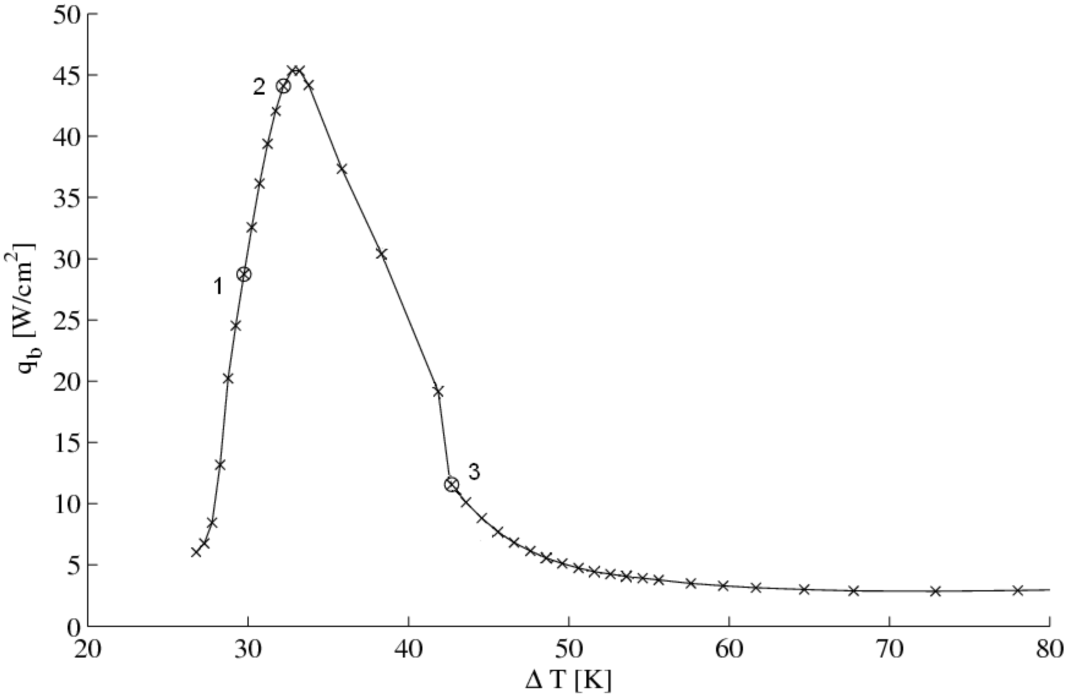

Fig. 12. Isopropanol boiling curve at $p_{sat} = 0.1$ MPa (adopted from [12])

We solve the 3D IHCPs along the isopropanol boiling curve (see Fig. 12). The measurement data at 36 MTCs have been taken with a sampling frequency of 25 kHZ [13]. Correspondingly, for the time discretization, time step size $\tau = 0.04$ ms in the one step θ-scheme is applied. The estimation time interval is chosen from 0 to 30 ms. Since there are more discretized mesh points (542) on Γ_M than MTCs (36), the temperature values at mesh points on Γ_M not corresponding to MTC positions are obtained by spatially interpolating the data measured at the 36 MTCs. The thermal diffusivity a and thermal conductivity λ are modeled as functions of the spatial coordinates to account for the fact that the heater is made of copper with thin sputtered gold (1 μm) layer on its top part [12]. The titanium layer (0.1 μm) is neglected. Due to space limitations, we only present the estimation results for three representative operating points 1, 2 and 3 in Fig. 12, which belong to the nucleate and transition boiling regimes. The macroscopic heat fluxes captured by the boiling curve at these three operating points are around 0.288 MW/m^2, 0.441 MW/m^2 and 0.108 MW/m^2, respectively. The operating point 2 is close to the point where the critical heat flux occurs.

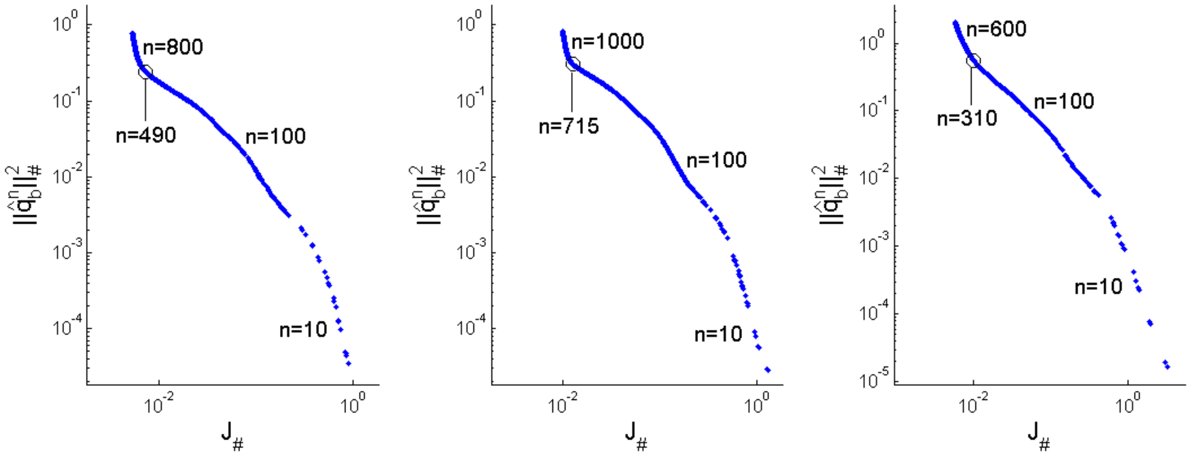

Fig. 13. L-curves for the data measured at operating point 1 (left), operating point 2 (middle) and operating point 3 (right).

By applying the L-curve criterion, the best estimated boiling heat fluxes for the three operating points are obtained at iteration 490, 715 and 310, respectively (see Fig. 13). The estimation results (see Fig. 14-22) show that the temporal and spatial evaluation of the surface heat flux differs significantly among the boiling regimes. Because of space limitations, we only show representative contour plots of estimated surface heat fluxes in special time intervals [22.24 ms, 22.52 ms], [10.96 ms, 11.24 ms] and [5 ms, 5.28 ms] for the three operating points, respectively (see Fig. 14-16). During these three short time intervals, the boiling heat fluxes above positions of MTC 22, 20 and 20 attain very high values, much higher than the values of macroscopic heat fluxes captured by the boiling curve shown in Fig. 12. The time evolution of estimated heat fluxes just above the MTC positions are shown in Fig. 17, 19 and 21 for the considered operating points. The estimated boiling heat fluxes above MTC positions 20-23 are compared with those obtained in [13] (see Fig. 18, 20, 22). Their peak values and patterns are consistent. However, we solve the IHCP in a 3D computational domain instead of a 2D one. Correspondingly, the estimation results are also extended from two to three space dimensions. In the following, we discuss the estimation results along the boiling curve in detail.

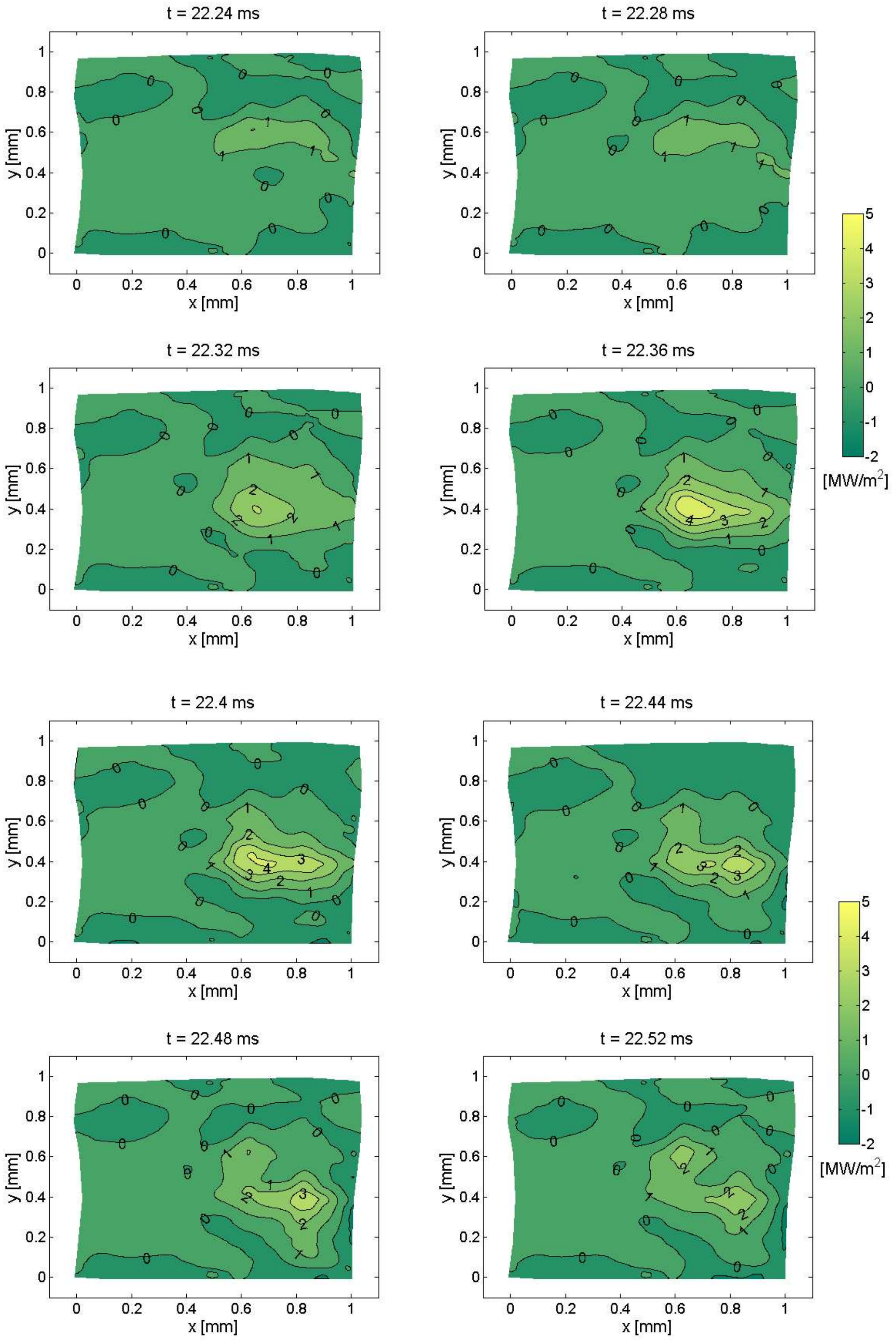

Fig. 14. Operating point 1 — contour plot of optimal estimated surface boiling heat flux in the time interval [22.24 ms, 22.52 ms].

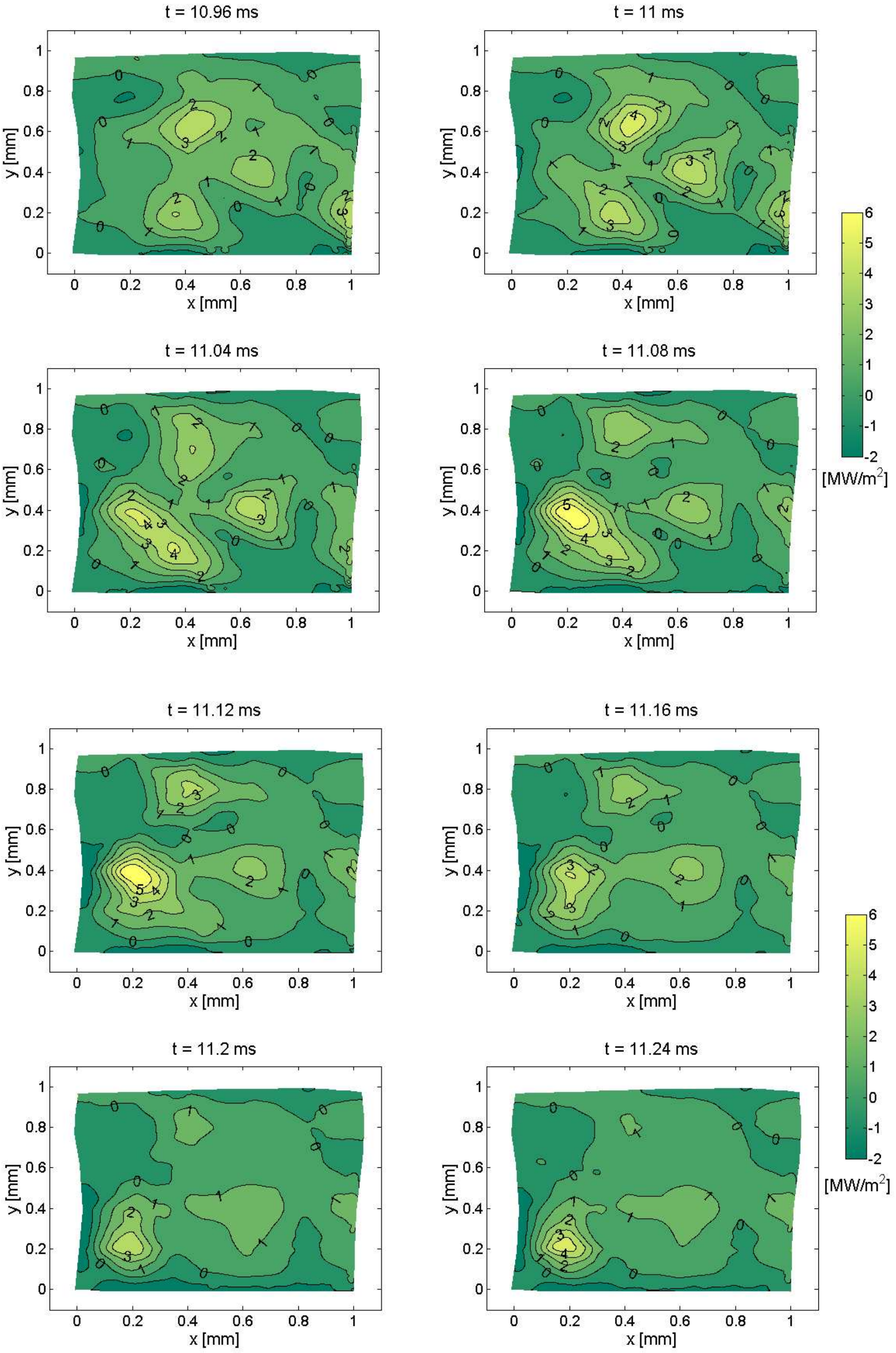

Fig. 15. Operating point 2 — contour plot of optimal estimated surface boiling heat flux in the time interval [10.96 ms, 11.24 ms].

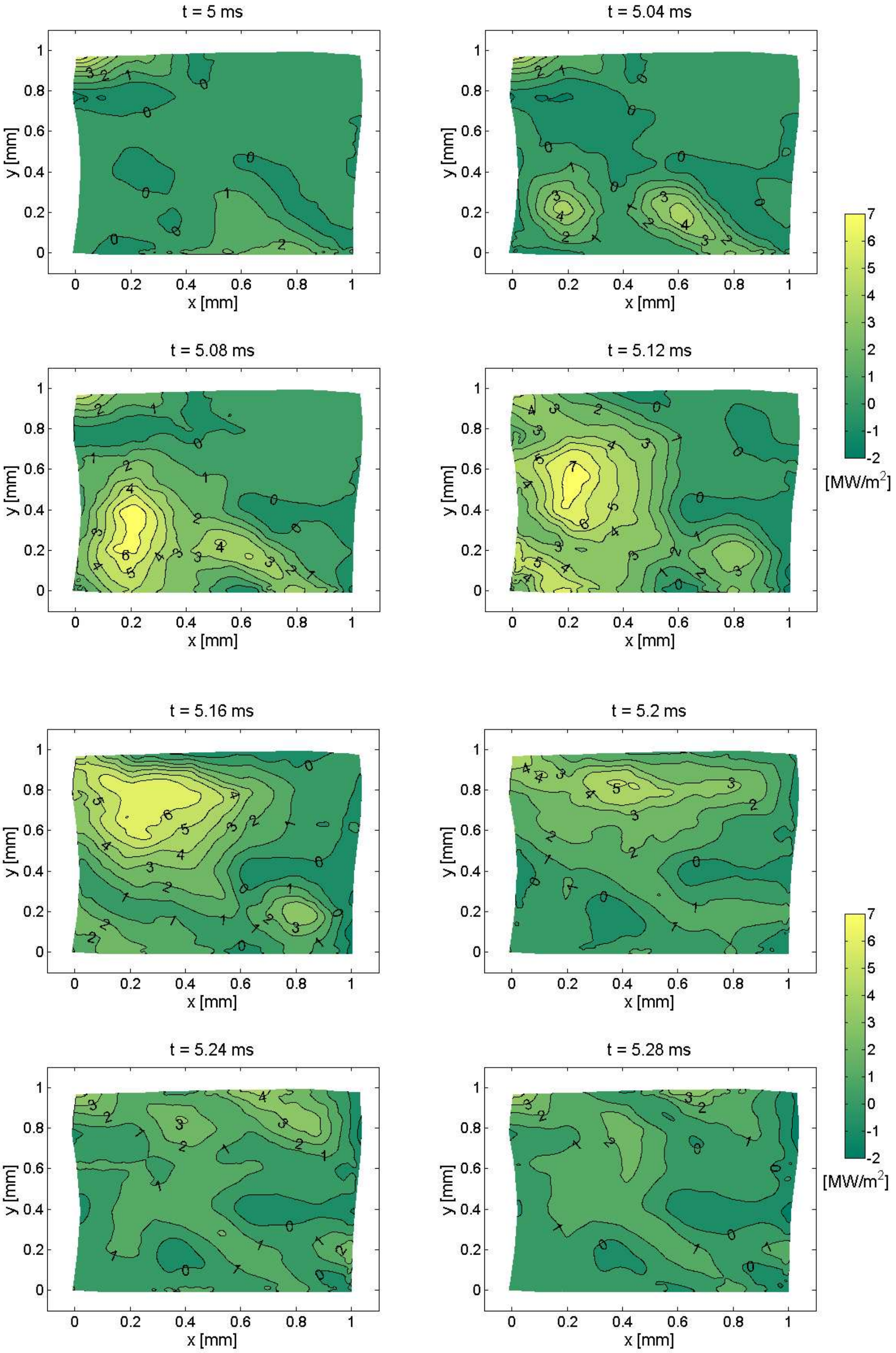

Fig. 16. Operating point 3 — contour plot of optimal estimated surface boiling heat flux in the time interval [5 ms, 5.28 ms].

In low heat flux nucleate boiling (results are not shown here), the temporal and spatial heat flux and surface temperature fluctuations are relatively moderate. The surface temperature exhibits fluctuations between 0.1-0.3 K.

At higher heat fluxes in nucleate boiling, e.g. at operating point 1, both the number of fluctuations per unit time and their amplitude increase. Frequent sharp temperature drops with amplitudes up to 1.0-1.5 K are observed. Fig. 17 shows the time evolution of the estimated heat fluxes above all the 16 MTCs which are not on the boundary of the heater volume. Peak values of the surface heat flux at this operating point reach up to 5-6 MW/m^2, which is much higher than the macroscopic value 0.288 MW/m^2. From Fig. 14 we can see that the boiling heat flux above MTC position 22 reaches its maximum at time instant $t = 22.36$ ms and the area of high heat fluxes covers only one or two observation positions above MTCs. Hence, the temperature and heat flux fluctuations at this operating point are probably caused by evaporating liquid-vapor structures such as nucleating bubbles with dimensions smaller than the size of MTC array.

At operating point 2, which is close to critical heat flux, both the fluctuations and the amplitudes of temperature drops continue to increase. Some longer periods of monotonically increasing temperature excursions up to 1.0-2.5 K can be observed to emerge in an irregular pattern. In addition, frequent sharp temperature drops with typical amplitudes up to 1.0-1.5 K can also be observed. Again, the temperature and heat flux fluctuations are probably caused by the local evaporation of liquid-vapor structures. This can also be confirmed by the estimation results shown in Fig. 15, where more local small areas with high heat fluxes are observed. Peak values of surface heat flux at this operating point reaches up to 6 MW/m^2 (see Fig. 19).

At operating point 3 and higher heat fluxes in transition boiling, the number of fluctuations per unit time decreases. However, larger temperature drops with amplitudes up to 2.0-3.0 K and temporal gradients of 10000 K/s are observed. Fig. 16 shows that the area of high heat fluxes is more extended compared to that in nucleate boiling. This indicates that the temperature and heat flux fluctuations become more correlated above the MTCs as the average superheat of the boiling surface is increased and these sharp temperature drops are probably due to a rewetting of the boiling surface. Fig. 21 shows the estimated heat fluxes above positions of 16 MTCs, which are not on the boundary of the heater volume. It also confirms the observation made from Fig. 16.

In summary, the time intervals with high temperature excursion continue to grow from high heat flux nucleate to transition boiling. Since time and space scales are coupled by the velocity of the wetting and rewetting process, longer periods of the temperature excursions mean larger structures of a possibly non-wetting area on the MTC array, due to the presence of a local vapour cluster for instance. Very similar patterns like the single fluctuation can be repeatedly identified at high heat flux transition boiling, e.g. at operating point 3. Generally, in high heat flux nucleate boiling at lower superheats, the amplitudes of the heat flux fluctuations are smaller than those observed in transition boiling. However, the number density of such temperature drops is much larger in the nucleate than in transition boiling. The magnitude and the number density of these fluctuations is therefore a feature of a particular boiling regime. In nucleate boiling the temperature drops and the associated high heat fluxes are certainly caused by rapid local evaporation at a nucleation site on the heater surface. In transition boiling, they are most likely caused by liquid contacts rewetting highly superheated and vapour-covered surface spots.

The characteristic sizes of the liquid-vapor structures in the two-phase at the surface are found to increase with increasing temperature superheats. Due to the spatial resolution of the MTCs, we introduced more spatial points on the measurement plane to ensure a reasonable accuracy of the discretized model. Interpolated temperature values at mesh points not corresponding to MTC positions are used for the numerical computation. We couldn't distinguish microlayer regions with high heat fluxes as observed in single bubble studies [10]. Similar to the estimation results in [13], negative heat fluxes in some time intervals at all three operating points are also found in our 3D estimation results (see Figs. 17-22). However, the time intervals in the 3D-case are very short. This may be an indication that there might locally exist heat transferred back to the heater surface, or an artefact of the numerical methods. The characteristics of temperature fluctuations in the different boiling regimes are associated with the dynamics of the two-phase layer above the heater surface. This has been measured with the same test heater by micro optical probes at different heights above the heater [35]. These measurements yield information about vapor-liquid structures and for some extent interface velocities of the two-phase structure above the surface.

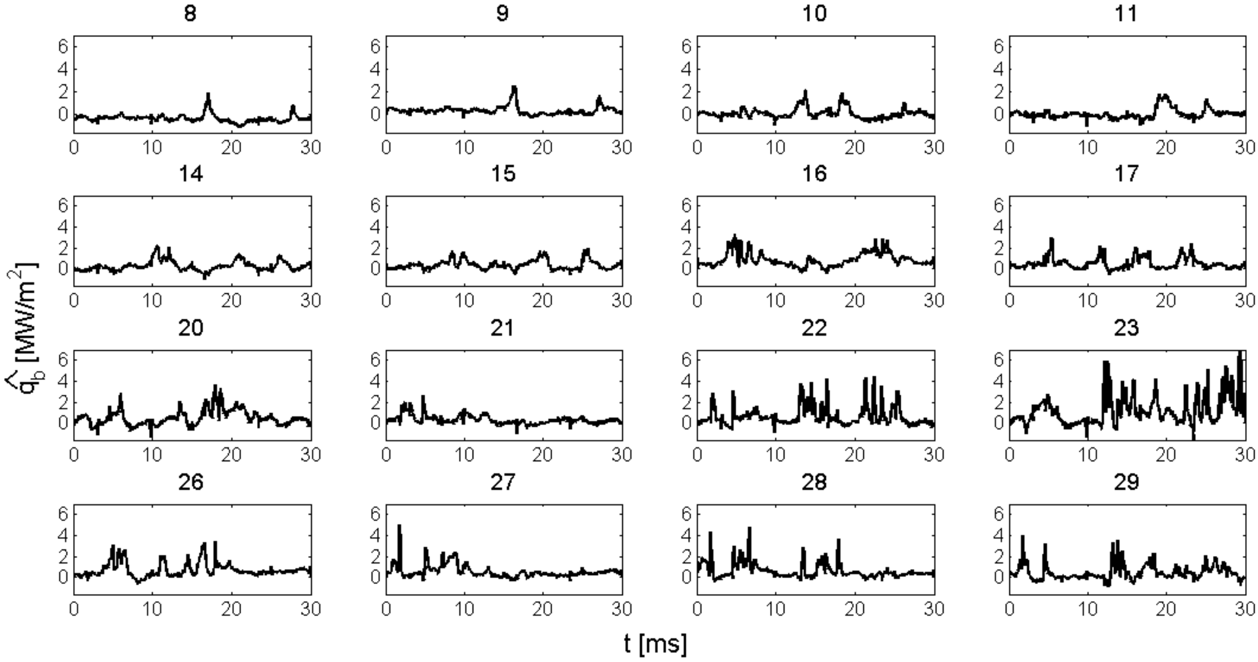

Fig. 17. Operating point 1 — optimal estimated boiling heat fluxes above MTC positions 8-11, 14-17, 20-23 and 26-29.

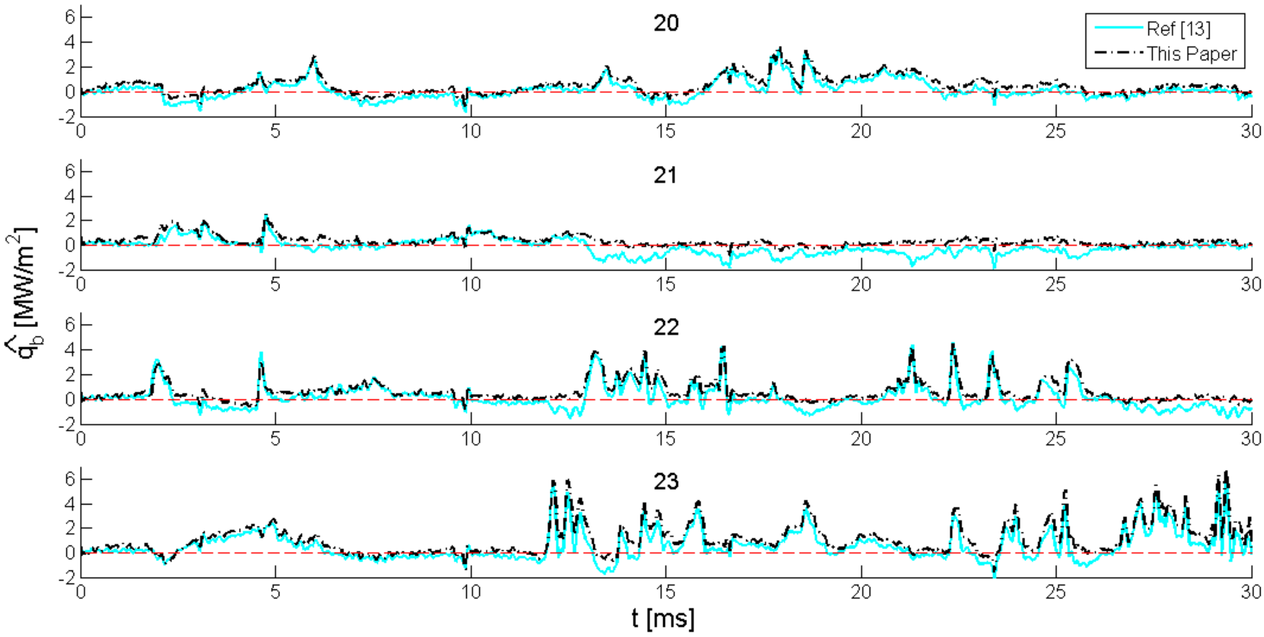

Fig. 18. Operating point 1 — a comparison of our estimated boiling heat fluxes above MTC positions 20-23 and those obtained in [13].

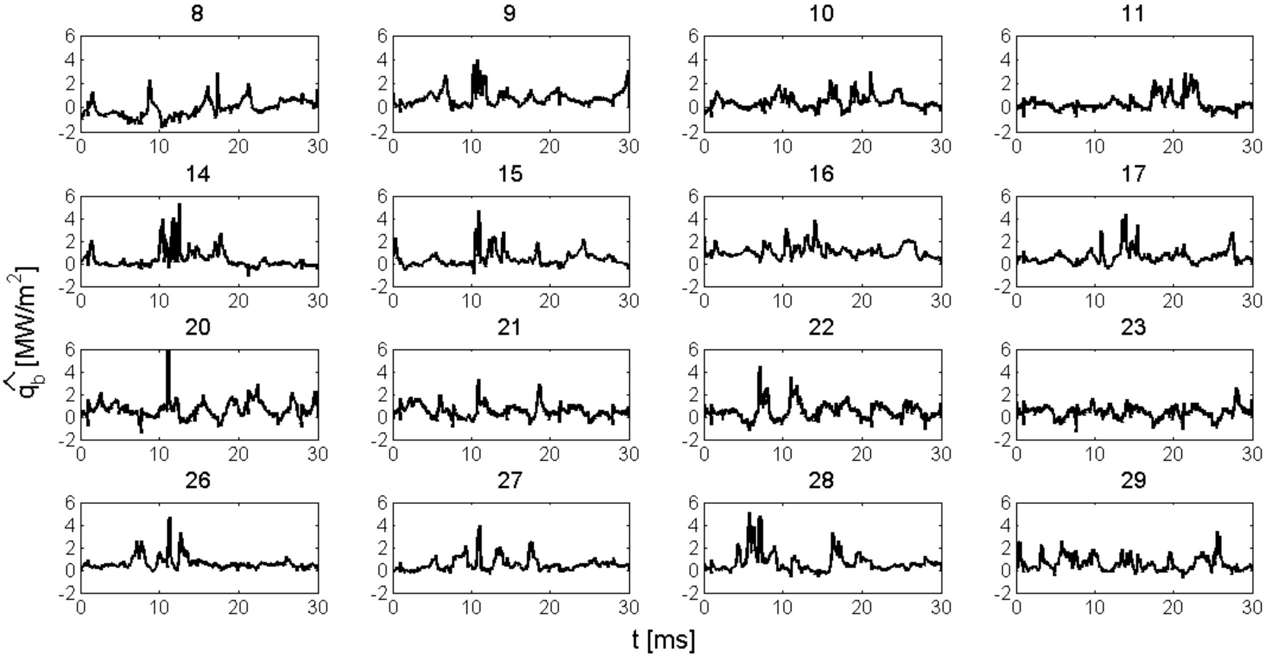

Fig. 19. Operating point 2 — optimal estimated boiling heat fluxes above MTC positions 8-11, 14-17, 20-23 and 26-29.

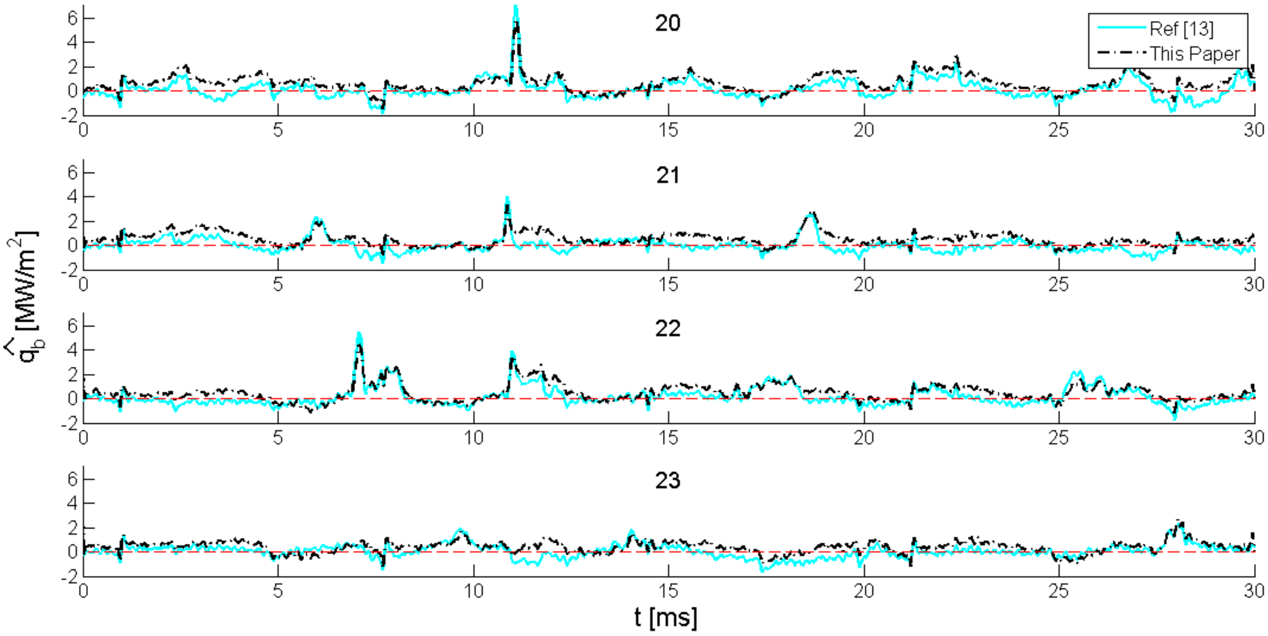

Fig. 20. Operating point 2 — a comparison of our estimated boiling heat fluxes above MTC positions 20-23 and those obtained in [13].

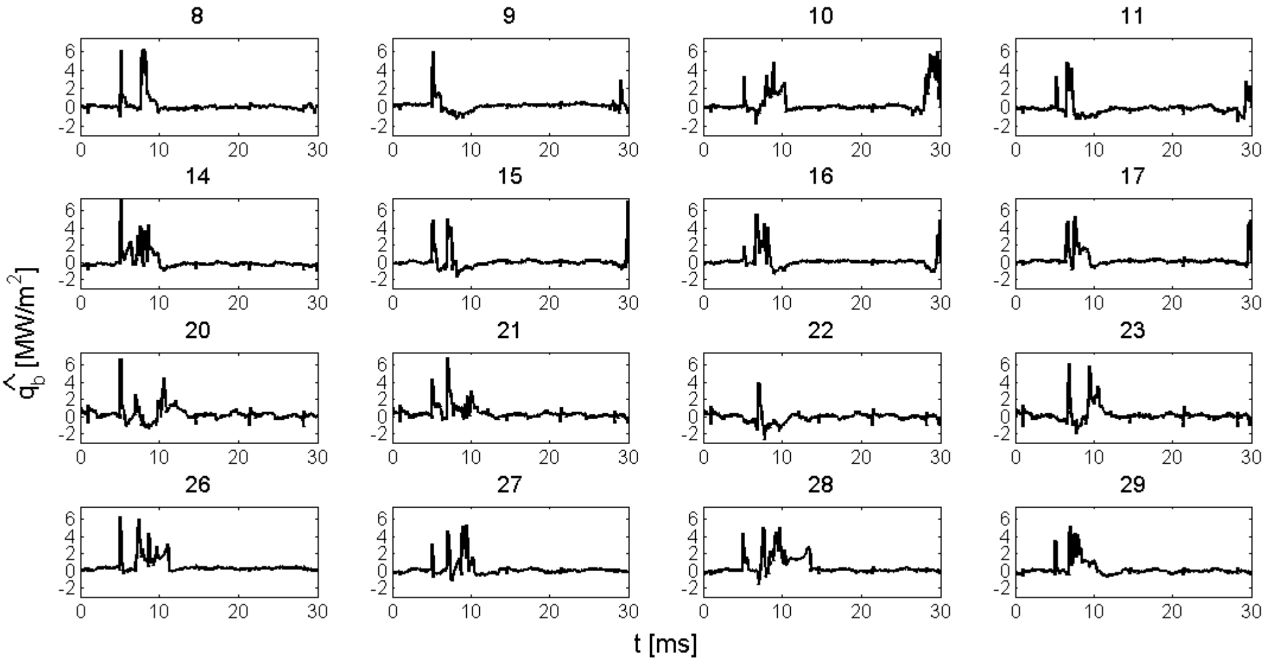

Fig. 21. Operating point 3 — optimal estimated boiling heat fluxes above MTC positions 8-11, 14-17, 20-23 and 26-29.

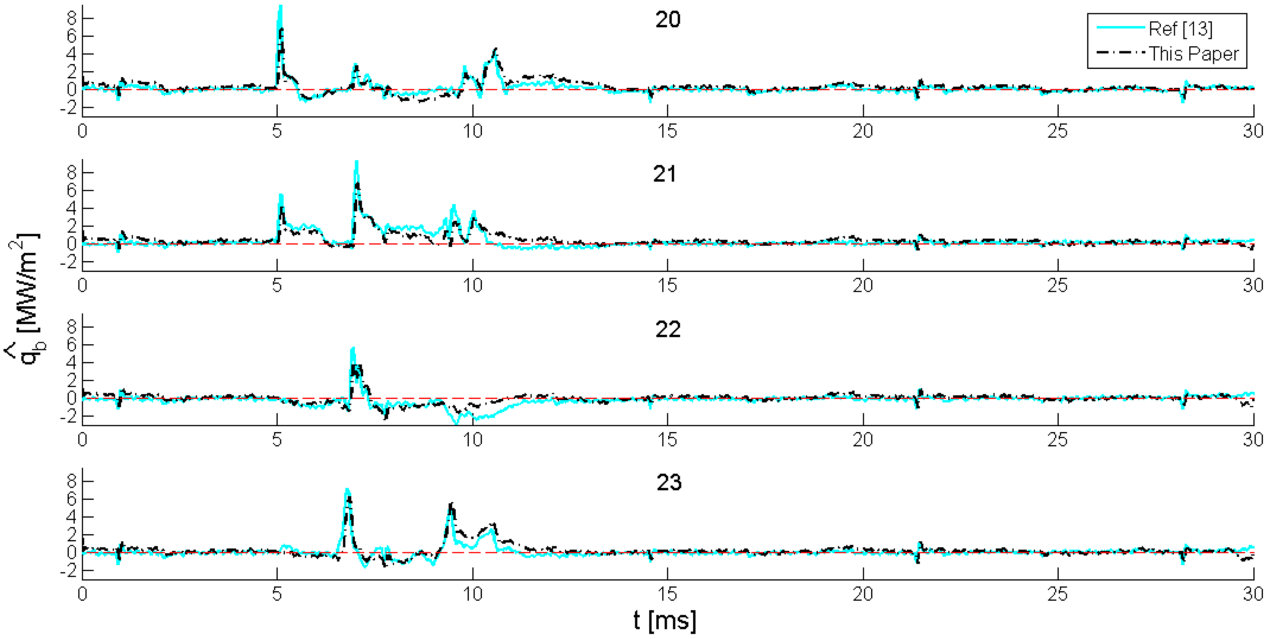

Fig. 22. Operating point 3 — a comparison of our estimated boiling heat fluxes above MTC positions 20-23 and those obtained in [13].

5 Conclusions

We have formulated and solved a transient IHCP on an irregular 3D domain in pool boiling experiments by applying a CG-based optimization method. A simulation case study has validated the solution approach. The local boiling heat fluxes at three representative operating points along the boiling curve of test fluid isopropanol have been successfully estimated. Using the CG-based solution approach, the computational bottleneck of the Filter-based method [24] for the given IHCPs in the pool boiling experiments has been overcome. Based on real experiments, the estimation results have been obtained for the first time in three space dimensions. The solution approach is rather general and can be used to solve similar 3D IHCPs at reasonable computational cost.

One of our future work will be devoted to the development of an appropriate strategy which can deal with limited measurements in space. Another possible improvement is to apply adaptive mesh refinement algorithms to find the optimal discretized model adapted to the identification task. This can avoid the inaccurate numerical computation with coarse discretized models and too much computation effort with an unnecessary fine one. Moreover, the identifiability issues will be addressed especially with respect to the spatial MTC resolution.

The characteristics of temperature fluctuations in the different boiling regimes are associated with the dynamics of the two-phase layer above the heater surface. The corresponding measurements obtained by micro optical probes [35] yield information about vapor-liquid structures and for some extent interface velocities of the two-phase structure above the surface. In combination with the associated heat flux distribution and dynamics evaluated in the present work, a data basis is available for the development of realistic mechanistic heat transfer models for boiling regimes beyond low heat flux nucleate boiling, where heat transfer models can be based on the study of single undisturbed bubbles.

Acknowledgement

The authors gratefully acknowledge the financial support by Deutsche Forschungsgemeinschaft DFG in the frame of a joint research project on fundamentals of boiling heat transfer and the graduate program GRK 775.

References

[1] John G. Collier and John R. Thome, Convective Boiling and Condensation, Oxford Engineering Science Series, No 38, 1996.

[2] S. G. Kandlikar, Handbook of Phase Change: Boiling and Condensation, Taylor & Francis, 1999.

[3] R.T. Lahey, A CFD analysis of multidimentional two-phase flow and heat transfer, In Process Enhanced and Multiphase Heat Transfer (A.E. Bergles Festschrift), pp. 431–441, Begell House, 1996.

[4] S.P. Antal, S. Nagrath and M.Z. Podowski, Multidimensional simulations of two-phase flows - in large volumes with injection spargers, In Proc. 4^{th} Int. Conf. Multiphase Flows ICMF 2001, May-June 2001, Paper 168.

[5] R. Krishna and J.M. van Baten, Modeling distillation tray hydraulics using CFD, In Proc. Conf. Transport Phenomena with Moving Boundaries, pp. 1–14, Berlin, October 2001.

[6] V.K. Dhir and S.P. Liaw, Framework for a unified model for nucleate and transition pool boiling, J. Heat Transfer 111 (3) (1989) 739–746.

[7] V.K. Dhir, Numerical simulations of pool-boiling heat transfer, AIChE Journal 47 (4) (2001) 813–834.

[8] R. Mei, W. Chen and J.F. Klausner, Vapor bubble growth in heterogenous boiling - I. formulation, Int. J. Heat Mass Transfer 38 (5) (1995) 909–919.

[9] R. Mei, W. Chen and J.F. Klausner, Vapor bubble growth in heterogenous boiling - II. growth rate and thermal fields, Int. J. Heat Mass Transfer 38 (5) (1995) 921–934.

[10] P. Stephan and J. Hammer, A new model for nucleate boiling heat transfer, Wärme- und Stoffübertragung 30 (1994) 119–125.

[11] V.P. Carey, Liquid-Vapor Phase-Change Phenomena, Series in Chemical and Mechanical Engineering, Hemisphere, 1992.

[12] M. Buchholz, H. Auracher, T. Lüttich and W. Marquardt, Experimental Investigation of Local Processes in Pool Boiling along the Entire Boiling Curve, J. Heat Fluid Flow 25 (2004) 243–261.

[13] T. Lüttich, Modeling and Identification of Pool Boiling Heat Transfer, Fortschritt-Berichte VDI, Nr. 847, VDI-Verlag, Düsseldorf, 2005.

[14] J. Beck, B. Blackwell and C. St. Clair, Inverse Heat Conduction. Ill-Posed Problems, Wiley, New York, 1985.

[15] O.M. Alifanov, Inverse Heat Transfer Problems, Springer, Berlin, 1994.

[16] J. Hadamard, Lectures on Cauchy's Problem in Linear Partial Differential Equations, Yale University Press, New Haven, 1923.

[17] A. N. Tikhonov and V. Y. Arsenin, Solutions of Ill-posed Problems, V. H. Winston and Sons, Washington, 1977.

[18] M. Raynaud and J. Bransier, A new finite-difference method for the nonlinear inverse heat conduction problem, Numer. Heat Transfer 9 (1986) 27-42.

[19] Y. Jarny, M. Ozisik and J. Bardon, A general optimization method using adjoint equation for solving multidimensional inverse heat conduction, Int. J. Heat Mass Transfer, 34 (11) (1991) 2911–2919.

[20] C. Yang and C. Chen, Inverse estimation of the boundary condition in three-dimensional heat conduction, J. Phys. D: Appl. Phys. 30 (15) (1997) 2209–2216.

[21] C.-H. Huang and S.-P. Wang, A three-dimensional inverse heat conduction problem in estimating surface heat flux by conjugate gradient method, Int. J. Heat Mass Transfer 42 (1999) 3387–3403.

[22] S. Chantasiriwan, An algorithm for solving multidimensional inverse heat conduction methods, Int. J. Heat Mass Transfer 44 (2001) 3823-3832.

[23] S. Groß, M. Soemers, A. Mhamdi, F. Al Sibai, A. Reusken, W. Marquardt and U. Renz, Identification of boundary heat fluxes in a falling film experiment using high resolution temperature measurements, Int. J. Heat and Mass Transfer 48 (2005) 5549–5562.

[24] T. Lüttich, A. Mhamdi and W. Marquardt, Design, Formulation and Solution of Multidimensional Inverse Heat Conduction Problems, Numer. Heat Transfer: Part B: Fundamentals 47 (2) (2005) 111–133.

[25] J. Blum and W. Marquardt, An optimal solution to inverse heat conduction problems based on frequency domain interpretation and observers, Numer. Heat Transfer: Part B: Fundamentals 32 (1997) 453–478.

[26] T. Lüttich, W. Marquardt, M. Buchholz and H. Auracher, Identification of Unifying Heat Transfer Mechanisms Along the Entire Boiling Curve, Int. J. Thermal Sciences 45 (2006) 284–298.

[27] A.C. Antoulas, Model reduction of largescale systems, SIAM, Philadelphia, 2004.

[28] S. Groß, J. Peters, V. Reichelt and A. Reusken, The DROPS Package for Numerical Simulations of Incompressible Flows Using Parallel Adaptive Multigrid Techniques, Technical Report No. 211, IGPM, 2002.

[29] H.W. Engl, M. Hanke and A. Neubauer, Regularization of Inverse Problems, Kluwer Academic Publishers, Dordrecht, 1996.

[30] J. Nocedal and S.J. Wright, Numerical Optimization, Springer, Berlin, Heidelberg, New York, 1999.

[31] K. W. Morton and D. F. Mayers, Numerical Solution of Partial Differential Equations, Cambridge University Press, Cambridge, New York, Melbourne, 1994.

[32] A. Quarteroni and A. Valli, Numerical Approximation of Partial Differential Equations, Springer, Berlin, Heidelberg, 1994.

[33] Y. Saad, Iterative Methods for Sparse Linear Systems, SIAM, Philadelphia, PA, USA, 2003.

[34] P. C. Hansen, Rank-Deficient and Discrete Ill-posed Problems: Numerical Aspects of Linear Inversion, SIAM, Philadelphia, 1998.

[35] M. Buchholz, H. Auracher, T. Lüttich and W. Marquardt, A Study of Local Heat Transfer Mechanisms Along the Entire Boiling Curve by means of Microsensors, Int. J. Thermal Sciences 45 (2006) 269–283.